Biophysical Journal
Article

Biophysical Society

Efficient Approximations for Stationary Single-Channel Ca^{2+} Nanodomains across Length Scales

Yinbo Chen,[1] Cyrill B. Muratov,[1] and Victor Matveev[1,*]
[1]Department of Mathematical Sciences, New Jersey Institute of Technology, Newark, New Jersey

ABSTRACT We consider the stationary solution for the Ca^{2+} concentration near a point Ca^{2+} source describing a single-channel Ca^{2+} nanodomain in the presence of a single mobile Ca^{2+} buffer with 1:1 Ca^{2+} binding. We present computationally efficient approximants that estimate stationary single-channel Ca^{2+} nanodomains with great accuracy in broad regions of parameter space. The presented approximants have a functional form that combines rational and exponential functions, which is similar to that of the well-known excess buffer approximation and the linear approximation but with parameters estimated using two novel, to our knowledge, methods. One of the methods involves interpolation between the short-range Taylor series of the free buffer concentration and its long-range asymptotic series in inverse powers of distance from the channel. Although this method has already been used to find Padé (rational-function) approximants to single-channel Ca^{2+} and buffer concentrations, extending this method to interpolants combining exponential and rational functions improves accuracy in a significant fraction of the relevant parameter space. A second method is based on the variational approach and involves a global minimization of an appropriate functional with respect to parameters of the chosen approximations. An extensive parameter-sensitivity analysis is presented, comparing these two methods with previously developed approximants. Apart from increased accuracy, the strength of these approximants is that they can be extended to more realistic buffers with multiple binding sites characterized by cooperative Ca^{2+} binding, such as calmodulin and calretinin.

SIGNIFICANCE Mathematical and computational modeling plays an important role in the study of local Ca^{2+} signals underlying vesicle exocytosis, muscle contraction, and other fundamental physiological processes. Closed-form approximations describing steady-state distribution of Ca^{2+} in the vicinity of an open Ca^{2+} channel have proven particularly useful for the qualitative modeling of local Ca^{2+} signals. We present simple and efficient approximants for the Ca^{2+} concentration in the presence of a mobile Ca^{2+} buffer that achieve great accuracy over a wide range of model parameters. Such approximations provide an efficient method for estimating Ca^{2+} and buffer concentrations without resorting to numerical simulations and allow us to study the qualitative dependence of nanodomain Ca^{2+} distribution on the buffer's Ca^{2+} binding properties and its diffusivity.

INTRODUCTION

Some of the most fundamental physiological cell processes such as synaptic neurotransmitter release, endocrine hormone release, muscle contraction, and cytotoxic immune cell response are directly and quickly triggered by the Ca^{2+} influx into the cytoplasm (1–4). Because of the diversity of Ca^{2+}-controlled cellular processes, intracellular Ca^{2+} signals are localized in time and space to allow selective activation of specific reactions (2–5). This localization is maintained in part by intracellular Ca^{2+} buffers, which absorb most of the Ca^{2+} influx soon upon its entry into the cell (6,7). In the context of secretory vesicle exocytosis, elevations of local Ca^{2+} concentration ($[Ca^{2+}]$) around individual Ca^{2+} channels or clusters of channels are termed Ca^{2+} nano- or microdomains (4,8). Although $[Ca^{2+}]$ can be measured experimentally using Ca^{2+}-sensitive dyes, inherent physical limitations pose challenges for optical Ca^{2+} imaging on small temporal and spatial scales relevant for vesicle exocytosis and other processes controlled by local Ca^{2+} elevations. Therefore, mathematical and computational modeling has played an important role in the study of vesicle exocytosis and other cell processes activated by localized Ca^{2+} signals (8–15). In particular, these computational studies were instrumental in showing that local Ca^{2+} elevations form and collapse very rapidly in response to

Submitted January 16, 2020, and accepted for publication June 10, 2020.
*Correspondence: matveev@njit.edu
Editor: Eric Sobie.
https://doi.org/10.1016/j.bpj.2020.06.038

channel gating. This suggests that quasistationary solutions of the reaction-diffusion equations describing Ca^{2+} influx, diffusion, and binding to intracellular Ca^{2+} buffers may achieve sufficient accuracy in estimating $[Ca^{2+}]$ in the vicinity of a Ca^{2+} channel, obviating computationally expensive solutions of partial differential equations describing buffered Ca^{2+} diffusion (16,17). Several of such stationary approximations have been introduced in the early works of Neher, Stern, Keizer, Smith, and others (14,18–28), most notably the excess buffer approximation (EBA), the rapid buffering approximation (RBA), and the linear approximation (LIN) (see Table 1). These approximations proved quite useful in understanding the properties of Ca^{2+} nanodomains and their dependence on the properties of cell Ca^{2+} buffers and are widely used in modeling studies (9,14,21,29–32). However, most of the previously developed approximations have two limitations: 1) their accuracy is restricted to specific regions in buffering parameter space, and 2) they have been developed for simple, 1:1 Ca^{2+}-buffer binding and are hard to extend to more realistic buffers that have multiple Ca^{2+} binding sites (33).

Here, we present several improved approaches allowing us to better approximate single-channel Ca^{2+} nanodomains with more accuracy and for a wider range of model parameters. One of these approximation methods is based on matching the coefficients of short-range Taylor series and long-range asymptotic series of the nanodomain Ca^{2+} distance dependence using simple ansätze. Although this method has already been used to obtain Padé (rational-function) nanodomain approximations (34), we show that significant improvement can be achieved in some parameter regimes using alternative interpolants that are similar in their functional form to EBA and LIN approximants. Similar ansätze can also be extended to buffers with multiple binding sites (data not shown). Apart from the local-series interpolation approach, we also present a different class of methods based on global optimization of a relevant functional with respect to parameters of the same ansätze that we use with the series interpolation method, which have superior accuracy in certain parameter regimes, as demonstrated below.

METHODS

Following prior work, we will consider a Ca^{2+} buffer whose molecules possess a single active site that binds a Ca^{2+} ion according to the reaction

$$B + Ca^{2+} \underset{k^-}{\overset{k^+}{\rightleftharpoons}} B^*, \tag{1}$$

where B and B^* are the free buffer and Ca^{2+}-bound buffer, respectively, and k^+ and k^- are the Ca^{2+}-buffer binding and unbinding rates. We consider a semi-infinite diffusion domain bounded by a flat plane containing point Ca^{2+} channel sources. Following previous modeling studies (18,19,27), we will assume Dirichlet boundary conditions on the outer boundary representing the background concentrations for Ca^{2+} and buffer in the bulk of the cell cytoplasm, and zero flux boundary condition on the flat boundary representing the cell membrane. Although this neglects Ca^{2+} pumps and exchangers along the flat boundary, numerical simulations show that qualitative agreement with more accurate models is retained under this assumption. The reflection symmetry along the flat boundary allows us to extend the domain to the whole space while doubling the source strength. Assuming mass-action kinetics, this yields the following reaction-diffusion system in $\mathbb{R}^3$ (18,19):

$$\begin{aligned}
\partial_t C &= D_C \nabla^2 C - k^+ B\, C \; + k^- B^* + 2 \sum_{k=1}^{N_{Ca}} \sigma_k \, \delta(\mathbf{r} - \mathbf{r}_k), \\
\partial_t B &= D_B \nabla^2 B \; - k^+ B\, C \; + k^- B^*, \\
\partial_t B^* &= D_B^* \nabla^2 B^* + k^+ B\, C \; - k^- B^*
\end{aligned} \tag{2}$$

Here, $C = [Ca^{2+}]$, B, and B^* represent concentrations of Ca^{2+}, free buffer, and Ca^{2+}-bound buffer, respectively, with diffusivities D_C, D_B, and D_B^*. In the source term, N_{Ca} denotes the number of Ca^{2+} channels, and the source strengths are given by $\sigma_k = I_{Ca,k}/(z\,F)$, where $I_{\mathrm{Ca,k}}$ are the amplitudes of individual open Ca^{2+} channels located at positions $\mathbf{r}_k$, F is the Faraday constant, and $z = 2$ is the valence of the Ca^{2+} ion. We note that the point-like channel assumption introduces inaccuracy at small spatial scales

TABLE 1 Previously Established Single-Channel Equilibrium Ca^{2+} Nanodomain Approximations

Method	Free Buffer Concentration, $b(r)$	Conditions	References
LIN	$1 + q\,[\exp(-r/\sqrt{q\lambda}) - 1]/r$	Linearization about $b = 1$	(14,19,22–26)
EBA	$1 + [\exp(-r\sqrt{\nu/\lambda}) - 1]/(\nu r)$	$\lambda >> 1$, $\nu >> 1$, $\lambda/\nu = O(1)$	(14,19,28)
IBA	$\eta\left[\frac{r}{1+\eta\, r} + \frac{\nu\, r^2}{(1+\eta\, r)^3} + \frac{2\lambda}{(1+\eta\, r)^4}\right]$	$\lambda << 1$, $\nu << 1$, $\lambda/\nu = O(1)$	(19)
RBA	$1 - \frac{1}{2q\nu}\left[1 + \frac{q}{r} - \sqrt{\left(1+\frac{q}{r}\right)^2 - \frac{4\nu q^2}{r}}\right]$	$\lambda << 1$, $\nu = O(1)$	(14,18–21,29)
RBA2	$b_{RBA}(r) + 2\lambda\eta[(1 + r/q)^2 - 4\nu\, r]^{-2}$	$\lambda << 1$, $\nu = O(1)$	(19)
Padé	$1 - q[r + (\sqrt{q(q+8\lambda)} + q)/2]^{-1}$	Series interpolation	(34)
Padé2	$\frac{r^2 + A_1(\lambda,\nu,\eta)r + A_2(\lambda,\nu,\eta)}{r^2 + B_1(\lambda,\nu,\eta)r + B_2(\lambda,\nu,\eta)}$	Series interpolation	(34)

For each method, only the free buffer concentration expression is shown because $[Ca^{2+}]$ can be found from the Ca^{2+} conservation law (Eq. 15). Note that LIN and EBA become identical in the limit $\nu >> 1$. RBA approximations valid up to orders O(1) and O(λ) are denoted as RBA (or $b_{\mathrm{RBA}}(r)$) and RBA2, respectively. The two lowest orders of the Padé method are denoted Padé and Padé2. For Padé2, the parameter-dependent constants $A_{1,2}$ and $B_{1,2}$ are given in Appendix C. The second-order EBA for $[Ca^{2+}]$ is derived in (19) and is not shown.

commensurate with the channel pore width of several nanometers. The impact of finite channel diameter and volumetric Ca^{2+} clearance was considered in a different type of single-channel stationary solution derived for the endoplasmic reticulum Ca^{2+} channel in (16).

The two linear combinations of Eq. 2 that cancel the reaction terms yield the conservation laws for the total Ca^{2+} and total buffer concentrations:

$$\partial_t(C+B^*) = \nabla^2\left(D_C C + D_B^* B^*\right) + 2\sum_{k=1}^{N_{Ca}} \sigma_k\, \delta(\mathbf{r}-\mathbf{r}_k) \quad (3)$$

and

$$\partial_t(B+B^*) = \nabla^2\left(D_B B + D_B^* B^*\right) \quad (4)$$

We now consider the steady state of this system, in which the conservation laws for Ca^{2+} and buffer reduce to (19–21,27,35,36)

$$D_B B + D_B^* B^* \;=\; D_B B_\infty + D_B^* B_\infty^* \;=\; const \quad (5)$$

and

$$\nabla^2\left[D_C\, C + D_B^* B^*\right] \;=\; -\,2\sum_{k=1}^{N_{Ca}} \sigma_k\, \delta(\mathbf{r}-\mathbf{r}_k) \quad (6)$$

Our approach is somewhat more general than prior modeling work in that we do not assume that buffer mobility is unaffected by Ca^{2+} binding. Given our simplifying assumptions on the domain geometry and boundary conditions, Eq. 6 has an exact solution:

$$D_C C + D_B^* B^* \;=\; \frac{1}{2\pi}\sum_{k=1}^{N_{Ca}} \frac{\sigma_k}{|\mathbf{r}-\mathbf{r}_k|} + D_C C_\infty + D_B^* B_\infty^*, \quad (7)$$

where C_∞ and B_∞ are the background values of C and B infinitely far from the channel, which are in equilibrium with each other:

$$B_\infty C_\infty \;=\; K\, B_\infty^* \quad (8)$$

Here, $K = k^-/k^+$ is the buffer affinity, equal to $[Ca^{2+}]$ at which half the buffer is bound at steady state. Conservation laws allow us to eliminate two variables, and we choose to retain the equilibrium free (unbound) buffer concentration as the remaining unknown:

$$D_B\, \nabla^2 B \;=\; k^+ B\, C \;-\; k^- B^* \quad (9)$$

We will now nondimensionalize these equations following (19) and (34), rescaling Ca^{2+} by the buffer affinity: $c = C/K$, $c_\infty = C_\infty/K$. However, we normalize buffer concentration by its background value B_∞ instead of total concentration. This will simplify our results, with many expressions formally unchanged whether or not $c_\infty = 0$ (see Table 1). Also note that in this case, a very simple relationship holds between background concentrations of Ca^{2+} and bound buffer: Eq. 8 yields $c_\infty = b_\infty^*$. We will consider the case of a single channel at the origin and rescale the spatial coordinate ($\mathbf{r}/L \to \mathbf{r}$) using the scale parameter that depends on the strength of the Ca^{2+} current, which simplifies the source term in Eq. 7 (19):

$$L = \sigma/(2\pi D_C K) \quad (10)$$

Recalling that $c_\infty = b_\infty^*$, we obtain the following nondimensional form of free buffer dynamics given by Eq. 9 and the conservation laws, Eqs. 5 and 7:

$$\begin{cases} \lambda\, \nabla^2 b \;\;\;\; = \;\; b\, c - b^*, \\ b + \delta_B^*\, b^* \;=\; 1 + \delta_B^*\, c_\infty, \\ c + \;\nu\, \delta_B^*\, b^* \;=\; c_\infty + \nu\, \delta_B^*\, c_\infty + 1/|\mathbf{r}| \;\;, \end{cases} \quad (11)$$

where the four nondimensional model parameters are (with L given by Eq. 10)

$$\lambda = \frac{D_B}{L^2\, k^-}, \quad \nu \;=\; \frac{B_\infty\, D_B}{K\;\; D_C}, \quad \delta_B^* \;=\; \frac{D_B^*}{D_B}, \quad c_\infty \;=\; \frac{C_\infty}{K} \quad (12)$$

Here, λ is the dimensionless buffer diffusion coefficient (denoted as ε_b in (19)), which quantifies the diffusion rate relative to the rate of Ca^{2+} binding and influx, and ν (denoted as $1/\mu$ in (19)) represents the overall buffering strength at rest, given by the product of the resting buffering capacity (B_∞/K) and the relative buffer mobility (D_B/D_C). In this nondimensionalization, unbuffered Ca^{2+} solution corresponds to $\nu = 0$ and has a simple form $c = 1/|\mathbf{r}| + c_\infty$. To simplify our results, we also introduce the following auxiliary parameters:

$$q = 1/(\eta+\nu), \quad \eta \;=\; c_\infty + 1/\delta_B^* \quad (13)$$

This allows us to specify the problem using only three parameters, either $\{\lambda, \nu, \eta\}$ or $\{\lambda, q, \eta\}$. In the special case of binding-independent buffer mobility ($\delta_B^* = 1$), η equals rescaled total buffer concentration: $(B_\infty + B_\infty^*)/B_\infty = 1 + c_\infty = \eta$.

Eliminating bound buffer and $[Ca^{2+}]$ using the two conservation laws in Eq. 11, the free buffer equation takes on a simple form:

$$\lambda\, \nabla^2 b \;=\; (b-1)(\nu b + \eta) + b/|\mathbf{r}| \quad (14)$$

$[Ca^{2+}]$ can be obtained from the solution of Eq. 14 using the Ca^{2+} conservation law in Eq. 11, which can be simplified to the following intuitive form:

$$c = \nu(b-1) + c_\infty + 1/|\mathbf{r}| \quad (15)$$

For $b < 1$, $[Ca^{2+}]$ is reduced in proportion to the buffering strength ν, as expected. The conservation laws in Eq. 11 along with the physical constraints $c \geq 0$, $b^* \geq 0$, $c_\infty \geq 0$ imply a priori bounds

$$\begin{aligned} &b_-(\mathbf{r}) \leq b(\mathbf{r}) \leq b_+(\mathbf{r}), \\ &b_-(\mathbf{r}) \;=\; \max\left(0,\;\; 1 - \nu^{-1}(c_\infty + 1\;/\;|\mathbf{r}|)\right), \\ &b_+(\mathbf{r}) \;=\; 1 + \delta_B^* c_\infty\,. \end{aligned} \quad (16)$$

Solutions satisfy the following boundary conditions (here and below, we denote $r = |\mathbf{r}|$):

$$\begin{cases} \lim\limits_{r\to 0} b(\mathbf{r}) \;=\; b_0 \;=\; \text{const}, \\ \lim\limits_{r\to +\infty} b(\mathbf{r}) \;=\; 1, \end{cases} \quad (17)$$

where the value of buffer at the source location, b_0, is unknown a priori. As is rigorously proved in Appendix D, Eq. 14 has a unique bounded solution satisfying these boundary conditions, and this solution is spherically symmetric. Therefore, Eq. 14 may be reduced to

$$E[b] \equiv \;-\;\frac{\lambda}{r^2}\,\frac{d}{dr}\left(r^2\frac{db}{dr}\right) + \;(b-1)(\nu b+\eta) + \;\frac{b}{r} \;=\; 0 \quad (18)$$

Although Eq. 18 superficially resembles the Lane and Emden-Fowler equations (37), it has no local Lie symmetries allowing analytical solution. Further, it is not of the Painlevé type (38) despite its simple algebraic form. We carried out the numerical solution of Eq. 18 using the relaxation method and the shooting method, cross-validating the results of these two methods. For certain extreme values of model parameters, accurate numerical solution is computationally intensive.

We note that the chosen nondimensionalization is identical to the one in (19,34) in the case of binding-invariant buffer mobility ($\delta_B^* = 1$) and zero background [Ca^{2+}] ($c_\infty = 0$). More generally, there is a simple equivalence with the nondimensionalization in (19,34); indicating variables in the latter work with the hat symbol, this equivalence reads

$$\widehat{\nu} = \nu\,\eta, \quad \widehat{b} = b/\eta, \quad \widehat{b}_\infty = 1/\eta \tag{19}$$

For the sake of simplicity, most numerical results shown below focus on the special case $c_\infty = 0$, $\delta_B^* = 1$, corresponding to $\eta = 1$ (Figs. 1, 2, 3, 4, 5, and 6). However, all results were verified for a wide range of η-values. In particular, results for $\eta = 10$ are shown in the results summary, Fig. 7.

One of the contributions of early modeling efforts was the development of accurate analytical approximations of the solution of Eq. 18. They allow avoiding computationally expensive integration of reaction-diffusion equations while retaining considerable accuracy (19,34). These approximations are summarized in Table 1, and apart from the Padé and LIN approximants, their regimes of applicability can be explained in intuitive physical terms. Namely, the EBA is applicable when buffer concentration is so large that it is practically unsaturable by the given Ca^{2+} current, leading to an additional exponential decay factor for [Ca^{2+}] with increasing distance from the channel (14,19,28,39). The RBA corresponds to the parameter regime in which the buffering rate is much faster relative to the diffusion rate, and at lowest order represents the condition for instantaneous equilibrium of the Ca^{2+} buffering reaction (14,18–21,29). The nearly immobile buffer approximation (IBA) is applicable in the case of small buffer mobility, implying in turn weak buffering strength (19). Finally, the LIN represents an ad hoc linearization around the free unbuffered point-source solution, $b = 1$, $c = 1/r + c_\infty$, but as Table 1 shows, LIN could also be viewed as an improved modification of the EBA. A more precise meaning of these approximants was given in Smith et al. (19). The latter work showed that EBA, RBA, and IBA represent asymptotic expansions in either λ or $\mu = 1/\nu$ and provided such expansions up to second order with respect to these parameters. Both LIN and RBA can be extended to multiple buffers and channels (21,24,33). In contrast, the Padé approximation (34) is based on a series matching method explained in detail below. We note that only second-order RBA and Padé approximations are comparable in accuracy to the approximants presented in this work in large regions of parameter space. Because [Ca^{2+}] is uniquely determined by the free buffer through the conservation law (Eq. 15), [Ca^{2+}] estimation accuracy is only shown in the final comparison of all approximations (see Figs. 5, 6, and 7). We note that accurate estimation of buffer concentration can be as important as the knowledge of the corresponding [Ca^{2+}] because it helps in the understanding of cell Ca^{2+} homeostasis and in interpreting the results of Ca^{2+} imaging, which requires quantifying Ca^{2+} binding to exogenously applied fluorescent Ca^{2+} buffers. Finally, we note recent work on time-dependent EBA (39).

RESULTS

Local properties of a stationary nanodomain

We start by generalizing some of the results previously presented in (34), without the restriction of binding-independent buffer mobility. We seek a solution to Eq. 18 that is bounded and analytic and therefore can be expanded in a Taylor series in r using a Frobenius-like method:

$$b(r) = b_o + \frac{b_o r}{2\lambda} + \frac{(b_0 - 1)(\nu\, b_o + \eta) + b_o/(2\lambda)}{6\lambda} r^2 + O(r^3) \tag{20}$$

The usefulness of this series by itself is limited because the value of buffer at the channel location, b_o, is a priori unknown, as mentioned above. Further, the convergence radius is finite because of the movable nonpole singularities of the solution in the complex r plane. However, the relationship

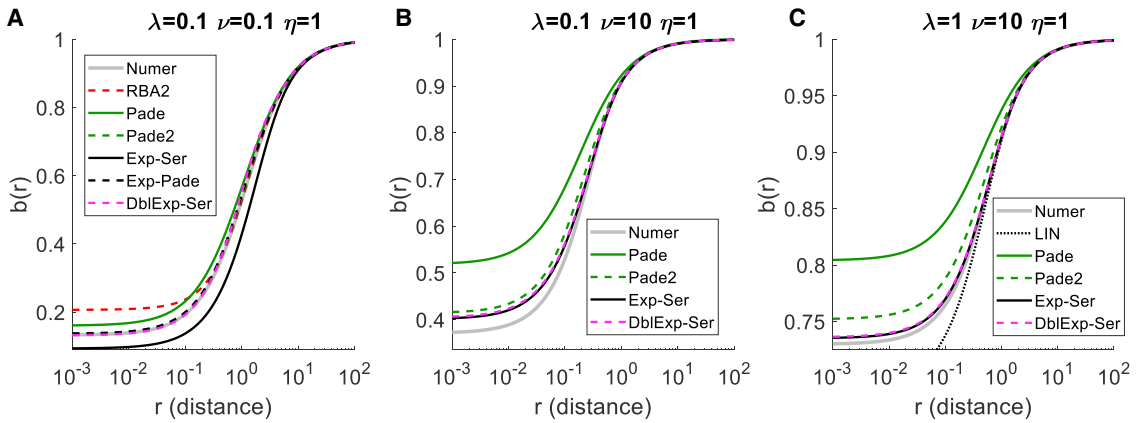

FIGURE 1 Comparison of equilibrium free buffer approximants obtained using series interpolation: first-order Padé (*green*), second-order Padé (Padé2, *dashed green*), Exp-Ser (*black*), Exp-Padé, (*dashed black*), and DblExp-Ser (*dashed magenta*). Also shown for comparison are RBA2 (*A*, *dashed red*) and LIN (*C*, *dotted black*). All panels show dimensionless buffer concentration as a function of distance from the Ca^{2+} channel for three distinct choices of model parameters λ and ν, with $\eta = 1$. Gray curves show the accurate numerical solution. In (*A*), DblExp-Ser, Padé2, and Exp-Padé are indistinguishable from the numerical solution at this resolution. Note that Exp-Padé does not yield a solution for $\nu > \eta = 1$ (*B* and *C*). In (*A*), DblExp-Ser curve shows the real part of Eq. 26. To see this figure in color, go online.

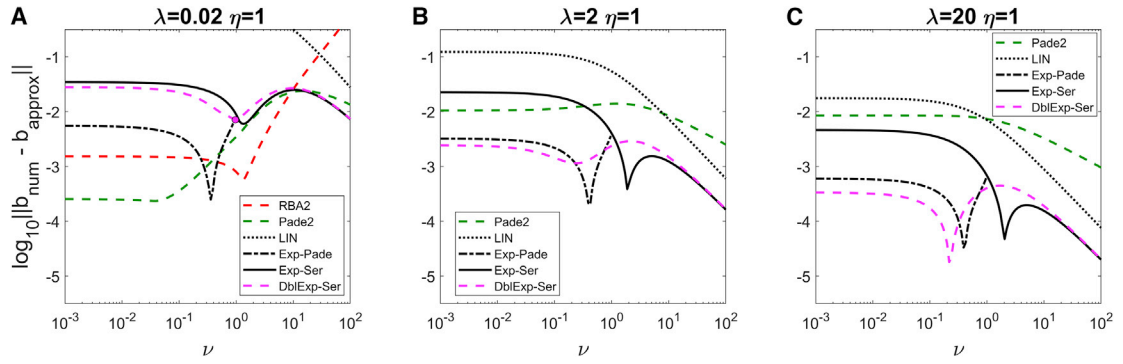

FIGURE 2 Accuracy comparison of equilibrium free buffer approximations obtained by series interpolation: Exp-Ser (*solid black*), Exp-Padé (*dashed black*), DblExp-Ser (*dashed magenta*), and Padé2 (*dashed green*). Also shown for comparison are RBA2 (*A, dashed red*) and LIN (*dotted black*). All curves represent the $\log_{10}$ of error norm given by Eq. 29 as a function of ν ranging from 10^{-3} to 10^{2} for three distinct choices of λ: $\lambda = 0.02$ (*A*), $\lambda = 2$ (*B*), and $\lambda = 20$ (*C*), with $\eta = 1$. Because Exp-Padé only yields a solution for $\nu < \eta = 1$, the corresponding curves terminate at $\nu = 1$. The magenta circle in (*A*) indicates the value of ν below which the exponent parameter α of DblExp-Ser becomes imaginary (see Fig. 6). For smaller values of ν, the magenta curve in (*A*) corresponds to the real part of Eq. 26. To see this figure in color, go online.

between Taylor coefficients in this expansion can be used to constrain parameters of an appropriately chosen approximation. Further, by making a coordinate mapping $x \equiv 1/r$, we transform our original Eq. 18 to the form

$$\lambda\, x^4 b_{xx} \;=\; (b-1)(\nu\, b+\eta) + bx \tag{21}$$

This reveals an essential singularity at $x = 0$. In fact, numerical study shows that the analytic extension of $b(x)$ to the complex-x plane has a branch cut across $x = 0$, jumping from the physical value $b = 1$ at $x = 0^{+}$ $(r \to +\infty)$ to the unphysical value $b = -\eta/\nu$ at $x = 0^{-}$ $(r \to -\infty)$ (see Fig. 7 in (34)). Among the approximants listed in Table 1, only RBA correctly captures this branch cut.

Given that the boundary condition infinitely far from the channel is known, $b(x = 0^{+}) = 1$, one can readily find the coefficients of a unique asymptotic power series expansion near $x = 0^{+}$:

$$\begin{aligned} b(x) \;=\; & 1 - qx + \eta\, q^3 x^2 + \eta(1 - 2q\eta) q^4 x^3 \\ & + \eta\big(2\lambda + 5\eta\, q^2(\eta\, q - 1)\big) q^4 x^4 + O\big(x^5\big). \end{aligned} \tag{22}$$

Here, we used parameter $q = 1/(\eta + \nu)$ to simplify the coefficients (cf. Eqs. 16 and 34 in (34)). Note that terms of this long-range expansion agree up to order $O(x^3)$ with RBA and up to order $O(x^5)$ with RBA2 (Table 1), indicating that the reaction is approximately at equilibrium far from channel.

The Padé method introduced in (34) and shown in Table 1 simultaneously matches leading terms of the two expansions given by Eq. 20 (containing unknown b_0 as a free parameter) and Eq. 22, using a simple rational-function interpolant,

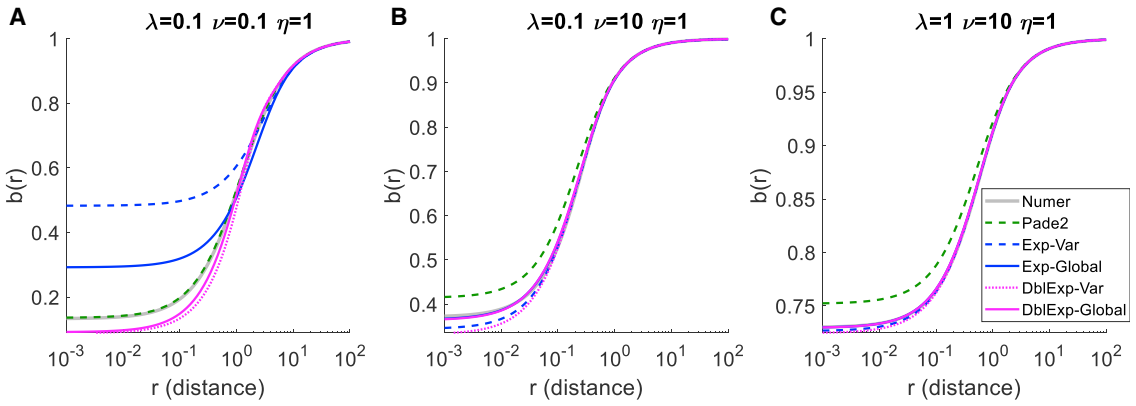

FIGURE 3 Comparison of equilibrium free buffer approximants obtained using the variational and the modified variational (global) methods: Exp-Var (*dashed blue curves*), DblExp-Var (*dotted magenta curves*), Exp-Global (*blue curves*), and DblExp-Global (*magenta curves*). Padé2 is also shown for comparison (*dashed green curves*). All panels show the free dimensionless buffer concentration as a function of distance from the Ca^{2+} channel for three distinct choices of model parameters λ and ν, with $\eta = 1$. Gray curves show the accurate numerical solution. In (*A*), the real part of DblExp-Var and DblExp-Global is shown. In (*B*) and (*C*), the curves for Exp-Global and DblExp-Global overlap the numerical solution. To see this figure in color, go online.

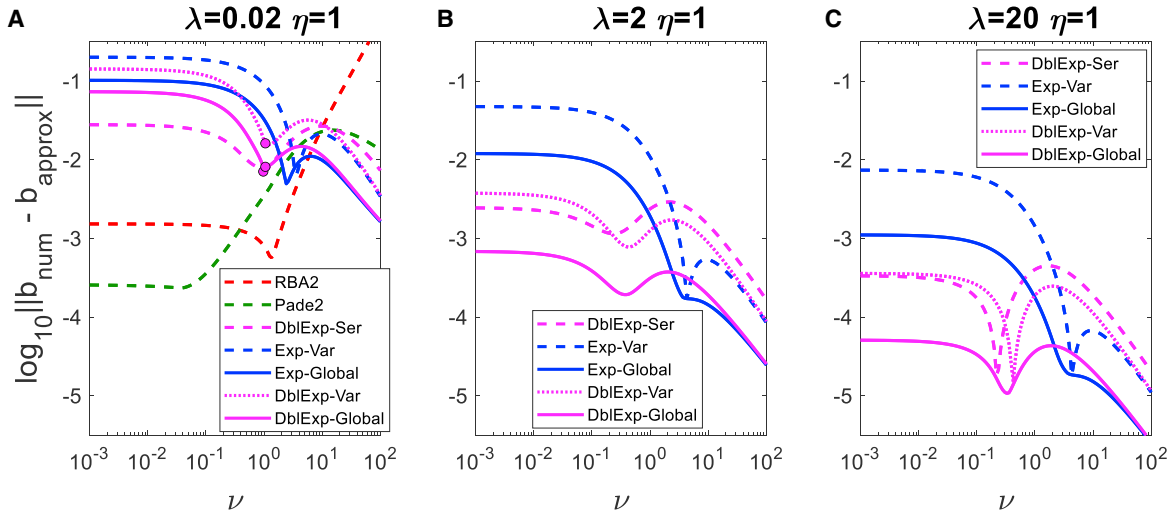

FIGURE 4 Accuracy comparison of equilibrium free buffer approximations obtained by the variational and modified variational (global) methods: Exp-Var (*dashed blue*), DblExp-Var (*dotted magenta*), Exp-Global (*blue*), and DblExp-Global (*magenta*). For comparison, also shown is the error of DblExp-Ser (*dashed magenta*), and (*A*) shows the errors of RBA2 (*dashed red*) and Padé2 (*dashed green*). All panels show $\log_{10}$ of the average error of free buffer approximation (Eq. 29) as a function of buffer strength ν ranging from 10^{-3} to 10^{2} for three distinct choices of λ: $\lambda = 0.02$ (*A*), $\lambda = 2$ (*B*), and $\lambda = 20$ (*C*), with $\eta = 1$. Magenta circles in (*A*) mark values of ν below which parameter α becomes imaginary for the corresponding DblExp method. For these smaller values of ν, the magenta curves in (*A*) correspond to the real part of Eq. 26. To see this figure in color, go online.

with coefficients found as functions of λ, ν (or q), and η. The simplest Padé interpolant of order 1 is

$$b\,(r) \;= 1 - \frac{q}{r+\beta},\;\; \beta = \frac{1}{2}\left[q + \sqrt{q(q+8\lambda)}\right]. \qquad (23)$$

This simple function satisfies Eqs. 20 and 22 to first order in r and x, respectively. The corresponding estimate of free buffer at the channel location is $b_0 = 1 - q/\beta$.

The Padé approximation was considered in (34) because of its algebraic simplicity and its straightforward expansion in power series in both r and $x = 1/r$. Therefore, it represents an ad hoc ansatz, and it is not necessarily the most natural nor the most accurate interpolant between the short-range and long-range power series given by Eqs. 20 and 22. Further, although it does converge to the true solution with increasing order, closed-form expressions for its coefficients can only be obtained for the two lowest orders in Table 1. However, we observe that all approximants in Table 1 can be viewed as interpolants between the Taylor series in r and asymptotic power series in $x = 1/r$, and therefore, the series interpolation method introduced in (34) should be

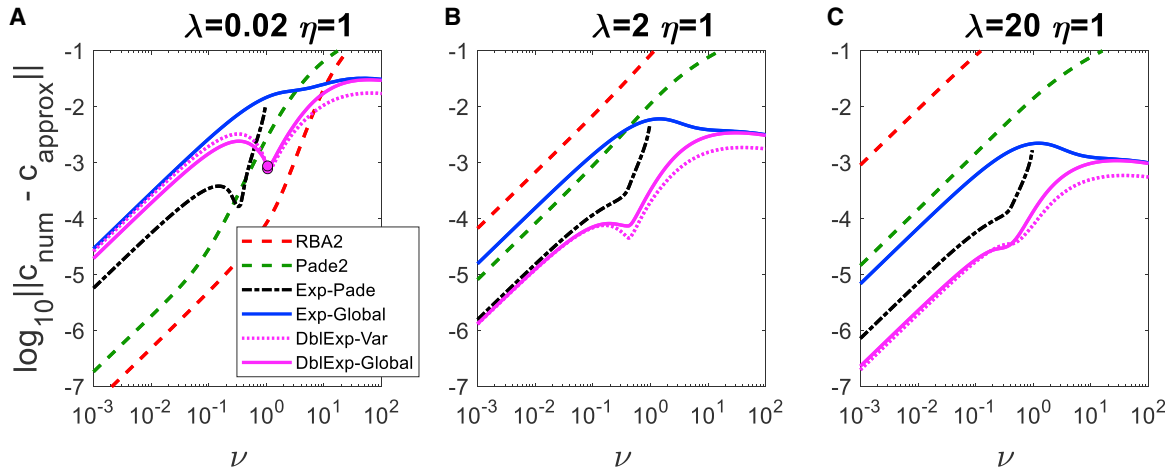

FIGURE 5 Accuracy comparison of equilibrium nanodomain $[Ca^{2+}]$ estimation by select approximants with smallest error: RBA2 (*dashed red*), Padé2 (*dashed green*), Exp-Padé (*dot-dashed black*), Exp-Global (*blue*), DblExp-Global (*magenta*), and DblExp-Var (*dotted magenta*). All panels show $\log_{10}$ of average absolute deviation of free dimensionless $[Ca^{2+}]$ (Eq. 36) as a function of buffering strength ν ranging from 10^{-2} to 10^{2} for three distinct choices of diffusivity parameter λ: $\lambda = 0.02$ (*A*), $\lambda = 2$ (*B*), and $\lambda = 20$ (*C*), with $\eta = 1$. Curves for Exp-Padé (*dashed black*) terminate at $\nu = \eta = 1$. To see this figure in color, go online.

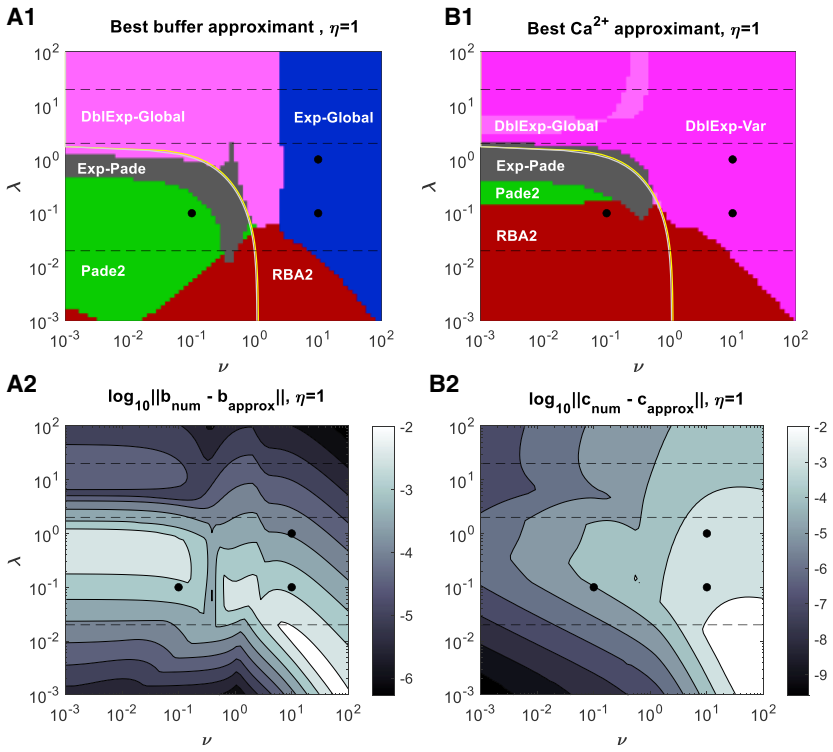

FIGURE 6 Parameter regions where a given approximant outperforms the rest in estimating (*A1*) free buffer and (*B1*) [Ca^{2+}] in the (ν, λ) plane, according to the error measures given by Eqs. 28 and 36. In all panels, $\eta = 1$. Colors indicate parameter region of best performance for each approximant: Padé2 (*green*), RBA2 (*maroon*), Exp-Padé (*gray*), DblExp-Var (*magenta*), DblExp-Global (*pink*), and Exp-Global (*blue*). Solid circles correspond to parameters in Figs. 1 and 3, and *dashed lines* corresponds to the parameter sweeps shown in Figs. 2, 4, and 5. Thin light semicircular curves indicate the boundaries inside of which the exponent parameters α in the DblExp-Var and DblExp-Global methods becomes imaginary (α is always real outside of the region marked by these curves for $\nu > 1$ and $\lambda > 1.8$). (*A2* and *B2*) The smallest error in estimating free buffer and [Ca^{2+}], respectively, achieved using the optimal approximants shown in (*A1*) and (*B1*). The grayscale in (*A2*) and (*B2*) indicates the $\log_{10}$ of error values given by Eqs. 28 and 36, respectively. Darker shade represents better accuracy. To see this figure in color, go online.

applied to the corresponding functional forms as well. Particularly promising in this respect are the simple exponential forms of the EBA and LIN, which are close to each other when $\nu >> 1$ and match in this limit the first two terms in the asymptotic expansion in Eq. 22, $b(x) = 1 - qx + O(x^2)$. In fact, standard analysis by substitution $b(x) = 1 - qx + \eta q^3 x^2 + e^{S(x)}$ reveals that in the limit $x = 1/r \to 0^+$, the general solution to Eq. 21 is described by

$$b(x) = 1 - qx + \ldots + C(x)x^{1+\sqrt{\frac{q}{\lambda}}\left(q-\frac{1}{2}\right)} e^{-\frac{1}{x\sqrt{q\lambda}}}, \qquad (24)$$

where $C(x)$ is bounded at $x = 0$. Apart from the fractional power of x, this expression has a similar form to EBA and LIN, suggesting that the corresponding functional form is a natural ansatz for describing long-range behavior of the solution.

Functional form of approximants

Given the above analysis, we introduce approximants that have a simple functional form inspired by EBA and LIN and that match the long-range asymptotic behavior of the solution, as given by Eqs. 22 and 24. Namely, we consider approximations in one of the following three parametric forms:

$$b(r) = 1 + q\frac{e^{-\alpha r} - 1}{r}, \qquad (25)$$

$$b(r) = 1 + q\frac{e^{-\alpha r} - 1}{r} - q^3\eta\frac{e^{-\alpha r}(1+\alpha r) - 1}{r^2}, \qquad (26)$$

$$b(r) = 1 + q\frac{e^{-\alpha r} - 1}{r} + q^3\eta\frac{1}{\beta + r^2} \qquad (27)$$

We refer to these approximants as exponential (Exp), double exponential (DblExp), and exponential-Padé (Exp-Padé), respectively. In the limit $r \to +\infty$ ($x = 1/r \to 0^+$), they explicitly satisfy Eq. 22 to either first or second order in x and are analytic at $r = 0$. The Exp and DblExp approximants depend on a single parameter α, whereas Exp-Padé contains an additional parameter β. Note that Eq. 25 reduces to LIN or EBA when α equals $(q\lambda)^{-1/2}$ or $(\mu\lambda)^{-1/2}$, respectively (see Table 1). The novelty of our approach is that we constrain the values of α and β using one of the following methods, described in detail further below:

1) Series interpolation: in this case, approximants in Eqs. 25 and 26 are referred to as Exp-Ser and DblExp-Ser, respectively.
2) Variational approach: Eqs. 25 and 26 in this case are referred to as Exp-Var and DblExp-Var.
3) Global (modified variational) approach: Eqs. 25 and 26 in this case are referred to as Exp-Global and DblExp-Global.

The value of parameter α is given by the solution of a quadratic equation for the exponential ansatz and a cubic equation for the double-exponential ansatz, as described in Tables 2 and 3. Parameters of the Exp-Padé approximant are defined by a fourth-order polynomial equation and are explicitly shown in Appendix B.

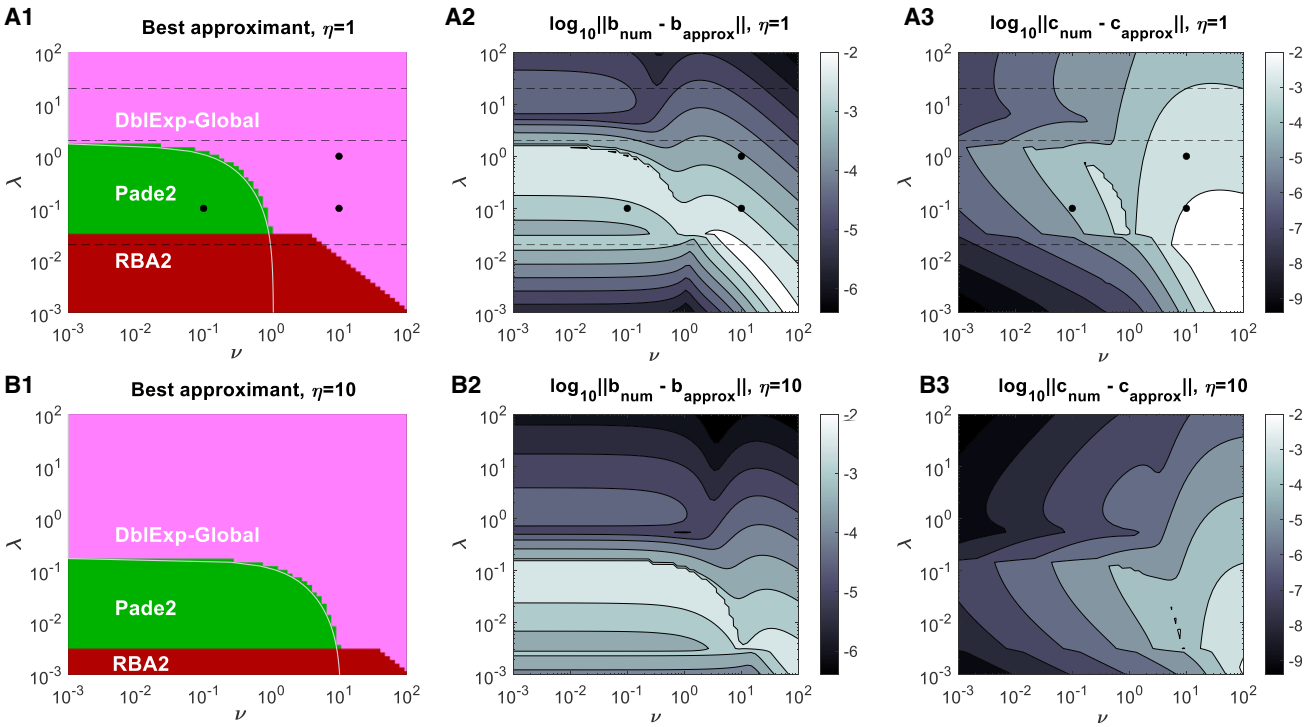

FIGURE 7 Simplified algorithm for choosing an optimal approximant, for two values of η: $\eta = 1$ (*A1–A3*) and $\eta = 10$ (*B1–B3*). (*A1*) and (*B1*): method choice as a function of ν and λ, according to the algorithm described in the text. Colors indicate optimal parameter region for each approximant: Padé2 (*green*), RBA2 (*maroon*), and DblExp-Global (*pink*). Solid circles in (*A1*)–(*A3*) correspond to parameters in Figs. 1 and 3, and dashed lines correspond to the parameter sweeps shown in Figs. 2, 4, and 5. Thin light semicircular curves mark boundaries inside of which the exponent α of the DblExp-Global approximant becomes imaginary. (*A2*) and (*B2*) and (*B3*) and (*A3*) show the smallest error in estimating free buffer and $[Ca^{2+}]$, respectively, achieved using the approximants chosen as indicated in (*A1*) and (*B1*). The grayscale in (*A2*) and (*B2*) indicates $\log_{10}$ of error values in Eqs. 28 and 36, respectively. The same grayscale is used for $\eta = 1$ and $\eta = 10$ for ease of comparison. To see this figure in color, go online.

Series interpolation approach results

For the simple exponential ansatz, Eq. 25, the relationship between the first two coefficients in the Taylor series in Eq. 20, $b_1 = b_0/2\lambda$, is satisfied for a unique value of exponent factor α given by a root of a quadratic equation, shown in Table 2: $\alpha = (\sqrt{1 + 4\lambda/q} - 1)/(2\lambda)$. The corresponding approximant will be referred to as Exp-Ser. Note that for $\lambda/q >> 1$, this reduces to LIN, given by $\alpha = (q\lambda)^{-1/2}$ (cf. Table 1).

A slightly more complex expression in terms of two exponentials, Eq. 26, allows us to match Eq. 22 to second order in x, $1 - qx + \eta q^3 x^2 + O(x^3)$. The relationship between the first two coefficients in the Taylor series in Eq. 20, $b_1 = b_0/2\lambda$, holds when the value of exponent factor α satisfies a cubic equation given in Table 3 and Eq. 37. This cubic has at most one real positive root for all values of parameters $\{\lambda, q, \eta\}$, which has an explicit solution shown in Appendix A. The corresponding approximant will be referred to as DblExp-Ser. We note that α becomes imaginary for sufficiently small λ and ν inside the parameter region marked by thin lines in Fig. 6, *A1* and *A2*; in that case, the real part of Eq. 26 will be used to compare it with other methods.

Finally, the ansatz given by Eq. 27 has an exponential term with parameter α and a rational term with parameter β. Two parameters allow us to match two relationships between the first three Taylor coefficients in the short-range series expansion, Eq. 20. This results in a polynomial system of order 4, with the level of complexity similar to that of Padé2 (34). This polynomial system and the explicit expression for its roots are provided in Appendix B. We note that the real positive solution for α and β is only possible when $\nu < \eta$ (equivalently, $2\eta\ q > 1$). In the limit $\nu \to \eta^-$, β diverges, and Exp-Padé approaches Exp-Ser.

TABLE 2 Equations for the Exponential Ansatz Parameter α

Exponent Parameter α in Eq. 25	LIN	Exp-Ser	Exp-Var	Exp-Global
$\alpha = \frac{\sqrt{S^2+\lambda/q}-S}{\lambda}$	$S = 0$	$S = \frac{1}{2}$	$S = \frac{1+2q\eta}{3}$	$S = \ln\frac{3}{2} + q\eta\ln\frac{4}{3}$

All monoexponential approximants described by Eq. 25 depend on a single parameter α that in turn depends on model parameters λ, q, and η through the same quadratic root formula, but with different values of constant S, as shown here.

TABLE 3 Equations for the Double-Exponential Ansatz Parameter α

Equation for Parameter α in Eq. 26: $\eta\, q^2 \boldsymbol{P}\alpha^3 - \boldsymbol{Q}\alpha^2 - \boldsymbol{R}\alpha + 1/q = 0$

	DblExp-Ser	DblExp-Var	DblExp-Global
P	$2\lambda/3$	$\lambda(8ln2-5) + \frac{4}{3}q^2\eta(1-\eta\, q)\left[1-3\ln\frac{4}{3}\right]$	$2\lambda(1-\ln2) + q^2\eta(1-q\eta)(\ln3-1)$
Q	$\lambda - \frac{q^2\eta}{2}$	$\lambda + \frac{2}{3}q^2\eta\left[1-6\ln\frac{9}{8} + 2q\eta\left(1-6\ln\frac{4}{3}\right)\right]$	$\lambda - 2q^2\eta\left(1-\ln\frac{81}{32} + 2q\eta\ \ln\frac{9}{8}\right)$
R	1	$(q\eta+2)/3$	$q\eta + 2(1-q\eta)\ln(3/2)$

All double-exponential approximants described by Eq. 26 depend on a single parameter α that, in turn, depends on model parameters λ, q, and η through the solution to a cubic equation of same form but with different values of polynomial coefficients P, Q, and R shown here. There is at most one positive real root of the cubic equation, given in Appendix A.

Fig. 1 compares these three approximants (Exp-Ser, DblExp-Ser, and Exp-Padé) with the previously developed Padé approximants of the two lowest orders, as well as RBA2 (Fig. 1 *A*) and LIN (Fig. 1 *C*). The accurate numerical solution is shown as a gray curve. For the parameters in Fig. 1 *A* ($\lambda = \nu = 0.1$), Exp-Ser is not as accurate as other approximants, but the accuracy of Exp-Padé and DblExp-Ser is excellent and comparable with that of Padé2; in fact, the three curves overlap the numerical solution curve. This is despite the fact that the value of α in DblExp-Ser is complex for $\lambda = \nu = 0.1$, so this is not an optimal parameter region for DblExp-Ser, and the real part of Eq. 26 is used in this case. For larger values of λ and/or ν in Fig. 2 *B* ($\lambda = 0.1$, $\nu = 10$) and 2 C ($\lambda = 1$, $\nu = 10$), approximants Exp-Ser and DblExp-Ser are more accurate than Padé and even Padé2. These results suggest that these series interpolants may be superior to previously developed approximants in a wide range of model parameters. Among previously developed approximants listed in Table 1, only RBA2 provides comparable accuracy when $\lambda < 1$ (Fig. 1 *A*).

Comparing the results by eye for several combinations of model parameters is clearly insufficient to unveil the parameter sensitivity of approximant accuracy. Therefore, following prior work (19,33,34), we explore parameter dependence of the absolute deviation between the given approximation b_{app} and the accurate numerical solution, b_{num}:

$$\|b_{app} - b_{num}\| = \frac{1}{N}\sum_{n=1}^{N}\left|b_{app}(r_n) - b_{num}(r_n)\right|, \qquad r_n = 10^{-3+5n/N},\quad n = 1,\ 2,\ \ldots N. \tag{28}$$

The deviations are computed on a set of $N = 100$ points spanning five orders of magnitude of distance r, from 10^{-3} to 10^{2}. Because we use exponentially spaced points, this norm is equivalent to an L^1 norm weighted by $1/r$, and therefore, it requires a short-range cutoff (we pick $r \geq 10^{-3}$). The higher weight at small r is justified by the fact that the short distance range is of greater interest, physically. Fig. 1 indicates that the chosen range of r is sufficient to capture the qualitative behavior of solutions for a wide range of parameter values. We checked that none of the conclusions are changed qualitatively by choosing an L^∞ norm instead.

The parameter dependence of this error norm is shown in Fig. 2, as buffering strength ν is systematically varied from 10^{-2} to 10^{2}, for three distinct values of λ. Each curve shows the error measure given by Eq. 28 for the corresponding approximation. For the sake of comparison, also shown are the error of Padé2 interpolant, the linear approximant (LIN), and RBA2 (Fig. 2 *A* only). For smaller values of λ (Fig. 2 *A*), Padé2 and RBA2 are still the superior approximation methods, but with increasing λ, the exponential approximants, Eqs. 25, 26, and 27, outperform all approximants in Table 1. Thus, the choice of the optimal approximation depends on the particular combination of model parameter values.

Variational approach

We now consider a completely different method of approximating solutions, based on a variational approach. As we rigorously demonstrate in Appendix D, the solution to Eq. 14 represents a unique minimizer of the following functional in an appropriate function space:

$$F[b] = \int_{\mathbb{R}^3}\left[\frac{\lambda}{2}|\nabla b|^2 + V(b,\mathbf{r}) - V(b_{RBA}(\mathbf{r}),\mathbf{r})\right] d^3r, \tag{29}$$

where $V(b, \mathbf{r})$ is defined by

$$V(b,\mathbf{r}) = -\eta b + \left(\frac{1}{|\mathbf{r}|} + \eta - \nu\right)\frac{b^2}{2} + \frac{\nu\, b^3}{3} \tag{30}$$

and $b_{\text{RBA}}(\mathbf{r})$ is the first-order RBA approximant given in Table 1, which solves Eq. 14 when $\lambda = 0$. Subtraction of $V(b_{\text{RBA}}(\mathbf{r}), \mathbf{r})$ in Eq. 29 is necessary to ensure boundedness of $F[b]$. Considering perturbations $b \to b + \varepsilon\phi$, where ϕ is a smooth function with compact support ($\phi \in C_c^\infty(\mathbb{R}^3)$), and denoting $V'(b, \mathbf{r})$ the first partial derivatives with respect to b, the variational derivative (the Gâteaux derivative) of $F[b]$ in the direction of ϕ is

$$D_\phi F[b] = \lim_{\varepsilon \to \infty} \frac{F[b+\varepsilon\phi] - F[b]}{\varepsilon}$$
$$= \int_{\mathbb{R}^3} \{\lambda \nabla b \cdot \nabla \phi + V'(b, \mathbf{r})\phi\} \; d^3 r$$
$$= \int_{\mathbb{R}^3} \left\{ \lambda \nabla b \cdot \nabla \phi + \left[(b-1)(\nu b + \eta) + \frac{b}{|\mathbf{r}|} \right] \phi \right\} \; d^3 r. \tag{31}$$

Therefore, setting

$$D_\phi F[b] = 0 \;\text{ for }\; \forall \phi \in C_c^\infty\left(\mathbb{R}^3\right) \tag{32}$$

formally yields the weak form (40) of Eq. 14. As is proved in Appendix D, the minimizer of $F[b]$ is unique and radially symmetric. Therefore, we seek an ansatz of the form $b(r; \alpha_k)$ and consider perturbations with respect to the ansatz parameters α_k, i.e., we take $\phi = \partial b(r; \alpha_k)/\partial \alpha_k$. Performing integration by parts in the derivative term transforms Eqs. 31 and 32 to

$$\frac{\partial F[b(r\,;\,\alpha_k)]}{\partial \alpha_k} = 4\pi \int_0^\infty E[b(r;\;\alpha_k)] \, \frac{\partial b}{\partial \alpha_k} r^2 \, dr = 0, \tag{33}$$

where $E[b]$ is defined in Eq. 18. For the ansatz given by Eqs. 25, 26, and 27, this integral may be computed in closed form, allowing us to obtain the optimal values of α_κ explicitly. For the lowest-order exponential ansatz (Eq. 25), considering $b(r; \alpha)$ with one free parameter in Eq. 33 leads to a quadratic equation for α with a unique positive real root, as given in Table 2. The corresponding approximant will be referred to as Exp-Var.

For the more complicated case of a double-exponential ansatz (Eq. 26), Eq. 33 leads to a cubic rather than a quadratic equation for α, analogously to the series interpolation method; this cubic is shown in Table 3, and its closed-form solution is given in Appendix A. This cubic has a single real positive real root for a wide range of model parameters $\{\lambda, \nu, \eta\}$, and we refer to the corresponding approximant as DblExp-Var. However, just like in the case of DblExp-Ser, α becomes complex when both λ and ν are sufficiently small. In this case, the real part of Eq. 26 still provides an accurate approximant. The performance of Exp-Var and DblExp-Var approximants will be investigated below, after considering our final approximation method.

Global method: modification of the variational approach

Given that Eqs. 25 and 26 represent narrow classes of functions that cannot provide a true minimum of $F[b]$, it may be useful to consider modifications of Eq. 33 that allow us to achieve a lower value of our chosen error norm, Eq. 28. One such modification is to replace the Jacobian factor r^2 in Eq. 33 with r, increasing contribution of small distances in this integral and thereby potentially reducing the error at short range:

$$\int_0^\infty E[b(r;\;\alpha)] \, \frac{\partial b}{\partial \alpha} r \, dr = 0 \tag{34}$$

We refer to this method of setting approximant parameter values as the "global" method or modified variational method. Eq. 34 can be rigorously obtained from the variational derivative given by Eqs. 31 and 32, but this time applied to perturbations ϕ of form

$$\phi(r) = \frac{1}{r} \frac{\partial b(r;\;\alpha)}{\partial \alpha} \tag{35}$$

Note that for the ansätze in Eqs. 25 and 26, this perturbation remains finite as $r \to 0$. Numerical results show that this modification does lead to noticeable improvement of the resulting approximants close to the channel location for many combinations of model parameters. In fact, for some parameter regimes, this method clearly outperforms the series interpolation and the variational approaches with respect to the weighted L^1 error measure given by Eq. 28.

For the lowest-order exponential ansatz (Eq. 25), after replacing $b(r; \alpha)$ in Eq. 34 with Eq. 25, one obtains a quadratic equation for α with a single positive real root given in Table 2; we refer to the corresponding approximant as Exp-Global. Just as in the case of the series interpolant method and the variational method, applying this method to the double-exponential ansatz (Eq. 26) leads to a cubic equation for parameter α, given in Table 3. We verified that this cubic has a single positive real root for a wide range of model parameters $\{\lambda, \nu, \eta\}$, and we refer to the corresponding approximant as DblExp-Global. However, like in the case of DblExp-Ser and DblExp-Var approximants, parameter α becomes imaginary when both λ and ν are sufficiently small; in that case, the real part of Eq. 26 will be used.

We note that a more straightforward approach of minimizing a weighted L^2 norm of $E[b]$ also leads to a closed-form solution in the case of a single-exponential ansatz, but the resulting approximant does not perform significantly better than the ones we present above, and it requires a solution of a more complicated fourth-order polynomial equation.

Accuracy of the variational and global approximants

Fig. 3 compares all variational and global approximants described above (Exp-Var, DblExp-Var, Exp-Global, and DblExp-Global) with Padé2 and the accurate numerical solution, using the same combination of model parameters as

in Fig. 1. It shows that in some cases (Fig. 3, *B* and *C*), the global approximations are more accurate than Padé2 and other series interpolants (cf. Fig. 1, *B* and *C*). Further, in Fig. 3, *B* and *C*, global approximants perform better than the corresponding variational approximants, and the differences between global methods and numerical results are barely noticeable. In contrast, Fig. 3 *A* illustrates that for $\nu = \lambda = 0.1$, none of the variational and global approximants are as accurate as Padé2, suggesting that the series interpolation methods may be superior for small values of ν and λ. We conclude that the variational and global approximants can be great improvements compared with the series interpolants in some, but not all, parameter regimes.

Fig. 4 shows a more systematic comparison to reveal the accuracy of the approximants obtained using the variational and the global methods in more detail. As in Fig. 2, buffer strength ν is varied from 10^{-2} to 10^{2} for three fixed values of dimensionless buffer diffusivity λ. Each curve shows the average absolute error in free buffer approximation, as given by Eq. 28. The error of the series interpolant DblExp-Ser is also included for comparison, and Fig. 4 *A* also shows the accuracy of RBA2 and Padé2. For small values of ν and λ (Fig. 4 *A*), RBA2, Padé2, and even DblExp-Ser are outperforming the variational approximants. However, as one increases the values of ν and λ, variational approaches are starting to show their advantage. For most parameter regimes, buffer approximations obtained using the modified variational (i.e., global) method are more accurate than the corresponding approximations obtained using the unmodified variational method. For example, in all panels of Fig. 4, Exp-Global is superior to Exp-Var.

We note that the second term in the DblExp approximants reflects the second term in the long-range asymptotic series, which scales as $q^3 = 1/(\eta + \nu)^3$; therefore, the double-exponential and the monoexponential ansätze approach each other when q is sufficiently small, corresponding to large values of buffer strength ν. This behavior of accuracy as $\nu \to \infty$ is apparent in Figs. 2 and 4.

Accuracy in approximating $[Ca^{2+}]$

As noted above, $[Ca^{2+}]$ is uniquely determined by equilibrium buffer concentration through the Ca^{2+} conservation law, Eq. 15. Nevertheless, it is useful to look separately at the accuracy of the Ca^{2+} estimation by the methods we present. Close to the channel location, $[Ca^{2+}]$ is dominated by the unbounded point-source term, $1/r$, and therefore, we will use a logarithmic error measure when comparing $[Ca^{2+}]$ approximations to our numerical solutions (19,33,34):

$$\| c_{app} - c_{num} \| = \frac{1}{N} \sum_{n=1}^{N} \left| \ln c_{app}(r_n) - \ln c_{num}(r_n) \right| \quad (36)$$

This sum extends over the same exponentially spaced points that were used for the buffer error measure given by Eq. 28, namely a set of 100 points spanning five orders of magnitude of distance. Fig. 5 plots this Ca^{2+} error measure for the optimal approximations that achieve the greatest accuracy over the wide range of parameters λ and ν. Because of the difference between the buffer and the Ca^{2+} error measures (cf. Eq. 28 vs. Eq. 36), the accuracy profile of different $[Ca^{2+}]$ approximants shown in Fig. 5 does not match perfectly the accuracy of the corresponding free buffer approximants shown in Figs. 2 and 4, despite the 1:1 relationship between the Ca^{2+} and free buffer concentrations. As explained above, the relative error in $[Ca^{2+}]$ estimation is particularly sensitive to the accuracy of the method at intermediate distances, rather than its accuracy in the vicinity of the channel, as is the case for the free buffer error measure (19,34). Note in particular that the DblExp-Var or DblExp-Global yield the most accurate Ca^{2+} approximations for $\lambda \geq 1$ (see Fig. 5, *B* and *C*), contrary to the error in buffer estimation, which is minimized by the Exp-Global and DblExp-Global approximants (cf. Fig. 4, *B* and *C*). However, for small values of λ, RBA2 and Padé2 are the best methods for estimating both $[Ca^{2+}]$ and buffer (Figs. 4 *A* and 5 *A*).

Summary and approximant selection algorithm

Fig. 6 summarizes all results presented in Figs. 1, 2, 3, 4, and 5, marking the best approximants and their errors over five orders of magnitude of buffer mobility λ and buffering strength ν. It shows that the methods we presented significantly improve the accuracy of approximation for a wide range of model parameters, and especially those corresponding to larger λ and ν. In fact, these methods outperform all previously developed approximants with the exception of RBA2 and Padé2 (19,34), which are still superior in wide regions of parameter space corresponding to small λ and small-to-moderate ν. Fig. 6, *A1* and *B1* can be used to design a simple algorithm for the selection of the optimal method. We find that such an algorithm can be further simplified by using just three methods, Padé2, RBA2, and DblExp-Global, with only a small sacrifice in accuracy. Below is the full sequence of steps allowing us to achieve good accuracy in the entire parameter range that we explored, combined with the steps needed to obtain final results in physical units:

1) Compute all nondimensional parameters (Eqs. 10, 12, and 13).
2) Find the nondimensional buffer concentration b using one of three methods:

a) If $\lambda\nu < 0.1$ and $\lambda\eta < 0.03$, then use RBA2 (Table 1).
b) Otherwise, use DblExp-Global if its parameter α is real (Eqs. 26, 37, 38, and 39).
c) Otherwise, use Padé2 (Table 1, Eqs. 43 and 44).

3) Compute nondimensional $[Ca^{2+}]$ using conservation law, Eq. 15.
4) Convert concentrations and distance to physical units: $[Ca^{2+}] = c\ K$, $[B] = b\ B_\infty$, $r \rightarrow r/L$.

In the last step, K denotes buffer's affinity, and B_∞ is the free buffer far from the channel (Eq. 8). Fig. 7 shows that the average error of the approximants chosen according to this simplified algorithm remains within 1% even for this simplified approach, for a very wide range of λ- and ν-values and two different values of η, namely $\eta = 1$ and $\eta = 10$. Note that the overall accuracy is increased at larger η-values, which corresponds to higher background $[Ca^{2+}]$ and/or reduced mobility of the Ca^{2+}-bound buffer state. Results in Fig. 6, *A1* and *B1* reveal that a somewhat better performance could be achieved if the buffer and Ca^{2+} approximations are chosen independently for a given set of parameter values, but this would lead to only a minor improvement. Apart from algorithm simplicity, choosing the same method for Ca^{2+} and buffer estimates guarantees that the conservation law, Eq. 15, is satisfied.

Finally, we note that another accurate buffer approximant can be obtained by applying the conservation law (Eq. 15) to the second-order EBA approximation for $[Ca^{2+}]$ derived in terms of exponential integrals in (19). This approximation has excellent performance relative to other methods when $\nu > 30$, in a certain range of λ-values. However, its accuracy advantage is significantly reduced when $\eta > 1$ and depends very steeply on the value of ν.

DISCUSSION

We presented a significant extension of prior modeling work on equilibrium single-channel Ca^{2+} nanodomains, based on two distinct approaches applied to several types of parametric approximants that, to our knowledge, have not been considered previously. In particular, we extended the series interpolation methods recently used to construct rational-function (Padé) approximants (34), generalizing it to more accurate and natural parametric forms given by Eqs. 25, 26, and 27, which bear resemblance to the EBA and LIN approximants obtained previously using different methods. Furthermore, we applied two versions of the variational approach to approximants of the same functional form, resulting in significant improvement of approximation accuracy for a wide range of parameters. As summarized in Figs. 6 and 7, a combination of previously developed and newly presented approximants can achieve an excellent estimation for the buffer and Ca^{2+} concentrations near an open channel for several orders of magnitude of model parameters λ, ν, and η. Further, we showed that a subset of just three methods, Padé2, RBA2, and DblExp-Global, allows us to achieve an average accuracy of 1% or better in the entire parameter range that we explored. As Figs. 6 and 7 show, the parameter region posing the greatest challenge corresponds to $\lambda << 1$, $\nu >> 1$. However, Figs. 1 *B*, 2 *A*, 3 *B*, 4 *A*, and 5 *A* illustrate that reasonable accuracy is achieved even in this parameter regime.

We note that the accuracy profiles shown in Figs. 2, 4, 5, 6, and 7 depend on our choice of the error measures, given by Eqs. 28 and 36. For instance, without spacing mesh points exponentially in these error measures, the accuracy ranking of different methods may change. However, this error measure choice provides a very demanding and restrictive comparison, covering a very wide range of distances and weighting the error more at short distances from the channel (19,33,34). Therefore, we believe that the chosen error measures are appropriate and yield the best comparison method given the wide range of parameters we consider. Further, we checked that the conclusions are not substantially changed if the L^∞ norm is chosen instead.

The drawback of the methods we present is that the expression for approximant parameters can be quite complex, especially for the ansätze with more than one exponential term. The level of complexity of different methods is not the same: the simplest ones are the monoexponential approximants (Exp-Ser, Exp-Var, and Exp-Global), followed by double-exponential methods that require finding a root of a cubic equation (DblExp-Ser, DblExp-Var, and DblExp-Global), and finally, two methods (Exp-Padé and Padé2) require solving a fourth-order polynomial system. However, all approximants were determined as closed-form expressions that only take several lines of computer code (see Appendices A, B, and C).

Several other functional forms were also considered but are not presented here because they either did not result in better accuracy compared to other approximants or provided only a minor improvement in limited regions of parameter space while complicating the expressions for parameters. This is true for example for the double-exponential approximation similar to Eq. 26 but with two different decay rates, α_1 and α_2. However, it is possible that we missed other accurate approximants. Such improved ansätze could be found, for instance, by taking into account the singularities of the analytic extension of the solution to the unphysical complex-distance plane. As we noted above, only RBA captures the branch cut of this analytic extension; further, RBA2 derived in (19) agrees with the long-range asymptotic expansion of the true solution given by Eq. 22 up to terms of order x^5 (34). Therefore, our initial efforts to construct an improved ansatz were focused on modifying RBA. However, so far, we have failed to find a modification that improves its performance.

More importantly, the presented approaches can be extended to the study of complex buffers with more realistic Ca^{2+} binding properties. Most prior modeling efforts, including this work, focused on a simple buffer with 1:1 Ca^{2+} binding, whereas most biological buffers possess several binding sites with distinct Ca^{2+} binding characteristics, for instance, calretinin and calmodulin (41–43). To date, only

RBA has been extended to such buffers, and only to first order (33). Our preliminary exploration reveals that the series interpolation approach can be extended to buffers with two binding sites, using a combination of rational and exponential functions, which is a subject of our work. Another direction of potential improvement is relaxing some of the key simplifying assumptions of the model, allowing for simple volumetric Ca^{2+} extrusion, considering Ca^{2+} channel pore of a finite width (16), and exploring the generalization of these methods to the case of two or more channels.

APPENDIX A: DOUBLE-EXPONENTIAL APPROXIMATION

Parameter α for each of the double-exponential ansätze described by Eq. 26 satisfies a cubic equation of the same form,

$$\eta\, q^2 P\alpha^3 - Q\alpha^2 - R\alpha + 1/q = 0, \tag{37}$$

where the polynomial coefficients P, Q, and R are given in Table 3. The three roots of this cubic can be succinctly represented in the following form:

$$\begin{aligned} \alpha_k &= \frac{1}{W}\left[Q - G_k - \frac{E}{G_k}\right], \\ &\begin{cases} W = 3\eta\, q^2 P, \quad E = Q^2 + WR, \\ F = \dfrac{3}{2}(QR - W/q)W + Q^3, \\ G_k = p_k\left[\sqrt{F^2 - E^3} + F\right]^{1/3}. \end{cases} \end{aligned} \tag{38}$$

The constants p_k ($k = 1, 2, 3$) in the expression for the intermediate quantity G_k denote branches of $(-1)^{1/3}$:

$$p_1 = \left(1 + i\sqrt{3}\right)\Big/2, \quad p_2 = \left(1 - i\sqrt{3}\right)\Big/2, \quad p_3 = -1 \tag{39}$$

In this notation, the real positive root of Eq. 37 corresponds to the value α_1 when implemented verbatim in MATLAB (The MathWorks, Natick, MA). For each of the three double-exponential approximants, the imaginary part of the root becomes nonzero for small values of ν and λ corresponding to the inner region marked by thin arcs in Fig. 6, *A1* and *B1*.

APPENDIX B: EXP-PADé APPROXIMATION

For the Exp-Padé ansatz (Eq. 27), matching the relationship between the first three terms in the Taylor series of the solution (Eq. 20) leads to the following algebraic system for the ansatz parameters α and β:

$$\begin{cases} \beta = \eta q^3[q\alpha(\lambda\alpha + 1) - 1]^{-1}, \\ (\alpha\beta)^2\dfrac{1 - 2\eta q}{2\eta\lambda q^2} + \alpha\beta\left(\alpha + \dfrac{2\eta q}{\lambda}\right) + 6 = \dfrac{\eta^2 q^3}{\lambda}. \end{cases} \tag{40}$$

This leads to a fourth-order polynomial equation for α, with the following explicit solution:

$$\alpha = \frac{1}{2\lambda}\left[H^{1/2} - Q + \left(\frac{2V}{H^{1/2}} - H - 6U\right)^{1/2}\right], \tag{41}$$

where constants U, V, H, and Q are determined by model parameters $\{\lambda, q, \eta\}$ according to

$$\begin{aligned} P &= 6 + \frac{\eta\, q^2(1 - \eta\, q)}{\lambda},\ Q = \frac{1}{P}\left(6 + \frac{\eta\, q^2}{2\lambda}\right), \\ R &= Q\left(1 - \frac{2\lambda}{q}\right) + \frac{2\eta^2 q^2}{P}, \\ U &= \frac{R}{3} - \frac{Q^2}{2},\ V = Q\left(R - Q^2\right) + \frac{12\lambda}{qP}, \\ W &= Q^2\left(\frac{R}{3} - \frac{Q^2}{4}\right) + 4\lambda\frac{6(Q + \lambda/q) - \eta^2 q^2}{3qP}, \\ E &= V^2\left(\frac{V^2}{4} + U\left(U^2 - 3W\right)\right) - W\left(W - 3U^2\right)^2, \\ G &= \frac{V^2}{2} + U\left(U^2 - 3W\right) + E^{1/2}, \\ H &= \frac{W + U^2}{G^{1/3}} + G^{1/3} - 2U. \end{aligned} \tag{42}$$

We note that the other three roots do not yield real positive values of α and β. In the parameter regime $1 - q\eta < 10^{-2}$ and $\lambda < 10^{-2}$, these expressions suffer from numerical loss of significance because of subtraction of values close in magnitude in several of the intermediate variables. The loss of accuracy can be corrected by an algebraic manipulation of the terms, by using higher-precision computation, or by applying a couple of Newton's iteration steps to the computed root value.

APPENDIX C: PADé2 APPROXIMATION

The Padé2 rational-function ansatz in Table 1 is obtained by series interpolation and leads to a fourth-order polynomial system (34), with the following exact solution for coefficients $A_{1,2}$ and $B_{1,2}$:

$$\begin{cases} B_2 = \dfrac{q}{R}\left(Q + G^{1/3} + \dfrac{H}{G^{1/3}}\right), \\ B_1 = \dfrac{1}{V}\left[\dfrac{B_2(B_2R - 3qK)}{6\lambda q^2} - J\right], \\ A_1 = B_1 - q, \\ A_2 = B_2 - q\left(B_1 - \eta q^2\right), \end{cases} \tag{43}$$

where constants Q, G, H, R, K, J, and $V$are determined by model parameters $\{\lambda, q, \eta\}$ and $p = q\nu$ according to

$$
\begin{aligned}
R &= 24\lambda - 3pq(p-2),\\
K &= 8\lambda^2 - 2\lambda q\left(2p^2-5p-2\right) - pq^2(p-2),\\
Q &= K + 24\lambda^2 - 4\lambda pq(2p-3),\\
V &= 2\lambda(p+6) + pq(p-3)(p-2),\\
F &= 6\lambda^2 - \lambda q(p+3)(p-2) - \eta p\, q^3(2p-3),\\
J &= 24\lambda^2 - 2\lambda pq(5p-8) - \eta p^2 q^3(p-2),\\
E &= 12\lambda^2 + \eta\, p\, q^2\left(8\lambda + \eta p\, q^2\right),\\
H &= p^2q^4(p-2)^2 + 1600\lambda^4 - 104\lambda^3 q(p-2)(9p+4)\\
&\quad +4\lambda^2q^2\left(39p^4-87p^3-63p^2+184p+4\right)\\
&\quad -4\lambda pq^3(p-2)\left(6p^3-21p^2+20p+2\right),\\
W &= 12000\lambda^5 - 4\lambda^4 q\left(2687p^2-2966p-553\right)\\
&\quad +4\lambda^3q^2\left(729p^4-1626p^3+486p^2+421p+70\right)\\
&\quad -\lambda^2q^3\left(243p^6-810p^5+609p^4+210p^3-21p^2-240p\right.\\
&\quad \left.-4\right) - 2\lambda\eta\, p\, q^5(p-2)\left(20p^2-13p-1\right) + p^2\eta^2q^7,\\
G &= Q^3 + 2\lambda R\left[3QF - 9\lambda ER + V(-3qW)^{1/2}\right].
\end{aligned}
\tag{44}
$$

The other three roots do not yield positive real values of coefficients $A_{1,2}$ and $B_{1,2}$ satisfying the constraints required for the correct physical behavior of the solution (34).

APPENDIX D: EXISTENCE AND UNIQUENESS OF SOLUTION

Here, we outline a rigorous mathematical study of Eq. 14 to establish the basic qualitative characteristics of its biophysically relevant solutions. The solutions of this equation must be understood in the distributional sense in $\mathbb{R}^3$ (40), in view of the fact that the right-hand side of Eq. 14 blows up at the origin, and therefore, the derivatives of $b(\mathbf{r})$ are undefined classically at $\mathbf{r} = 0$. We will take advantage of the variational formulation, Eqs. 29, 30, 31, and 32, to establish the basic existence, uniqueness, regularity, and symmetry properties of the solutions of the above equation in the physically relevant class of functions b: $\mathbb{R}^3 \to \mathbb{R}$, namely functions that approach the limit at infinity sufficiently fast and obey the bounds in Eq. 16. To make the statement in Eqs. 29, 30, 31, and 32 more precise, we need to ensure that $F[b]$ is well defined and differentiable for a given b. A natural class of functions ensuring these conditions is the homogeneous Sobolev space $\mathring{W}^{1,2}(\mathbb{R}^3)$, i.e., the space of locally integrable functions with square integrable first weak derivatives (for the basic notations and the definitions of the function spaces used below, see (40,44)). This makes the first term in the integrand in Eq. 29 well defined. Nonetheless, we still need to make sure that the rest of the integrand does not give rise to a divergent integral due to a possible slow decay of $b(\mathbf{r}) - 1$ as $\mathbf{r} \to +\infty$. To control the latter issue, we invoke Eq. 16. For simplicity of notation, let $V'(b, \mathbf{r})$ and $V''(b, \mathbf{r})$ denote the first and the second partial derivatives with respect to b. Taylor expanding around $b_{\mathrm{RBA}}(\mathbf{r})$ and taking into account that $V'(b_{RBA}, \mathbf{r}) = 0$, we have

$$
V(b,\mathbf{r}) = V(b_{RBA}(\mathbf{r}),\ \mathbf{r}) + \frac{1}{2}V''\left(\tilde{b}(\mathbf{r}),\mathbf{r}\right)\left(b - b_{RBA}(\mathbf{r})\right)^2
\tag{45}
$$

for some $\tilde{b}(\mathbf{r})$ lying between $b(\mathbf{r})$ and $b_{\mathrm{RBA}}(\mathbf{r})$. We note that $b_{\mathrm{RBA}}(\mathbf{r})$ satisfies the bounds in Eq. 16, obeys $b_{\mathrm{RBA}}(\mathbf{r}) \sim |\mathbf{r}|$ as $|\mathbf{r}| \to 0$, and agrees up to order $O(|\mathbf{r}|^{-3})$ with Eq. 22 as $|\mathbf{r}| \to +\infty$. Because $\tilde{b}$ also satisfies the bounds in Eq. 16 and because

$$
V''\left(\tilde{b},\mathbf{r}\right) = \eta - \nu + 1/|\mathbf{r}| + 2\nu\tilde{b},
\tag{46}
$$

we obtain from Eq. 46 and the definition of η (Eq. 13) that

$$
V''\left(\tilde{b},\mathbf{r}\right) \geq \eta - c_\infty = 1/\delta_B^* > 0
\tag{47}
$$

In particular, F is non-negative in the considered class. Also, by inspection, $b_{RBA} \in \mathring{W}^{1,2}(\mathbb{R}^3)$. Therefore, it holds that

$$
F[b_{RBA}] < +\infty,
\tag{48}
$$

indicating that F is finite on a nonempty subset of $\mathring{W}^{1,2}(\mathbb{R}^3)$, satisfying the bounds in Eq. 16.

We now proceed with establishing existence of solutions of Eq. 14 that are minimizers of F among all $b \in \mathring{W}^{1,2}(\mathbb{R}^3)$ satisfying Eq. 16. To this aim, we first redefine F to relax the constraints in Eq. 16, by introducing

$$
\tilde{F}[b] = \int_{\mathbb{R}^3}\left[\frac{\lambda}{2}|\nabla b|^2 + \tilde{V}(b,\ \mathbf{r}) - V(b_{RBA}(\mathbf{r}),\ \mathbf{r})\right] d^3r,
\tag{49}
$$

where

$$
\tilde{V}(b,\mathbf{r}) = \begin{cases} V'(b_-(\mathbf{r}),\mathbf{r})(b - b_-(\mathbf{r})), & b < b_-(\mathbf{r}),\\ V(b,\mathbf{r}), & b_-(\mathbf{r}) \leq b \leq b_+(\mathbf{r}),\\ V'(b_+(\mathbf{r}),\mathbf{r})(b - b_+(\mathbf{r})), & b > b_+(\mathbf{r}). \end{cases}
\tag{50}
$$

Notice that $\tilde{F}[b] = F[b]$ for all b satisfying Eq. 16. Also, by inspection, $\tilde{V}(\ \cdot\ ,\ \mathbf{r}) \in C^{1,1}(\mathbb{R})$ for all $\mathbf{r} \neq 0$ and

$$
V'(b_-(\mathbf{r}),\ \mathbf{r}) < 0, V'(b_+(\mathbf{r}),\ \mathbf{r}) > 0
\tag{51}
$$

In particular, $\tilde{V}(b, \mathbf{r}) \geq V(b_{RBA}, \mathbf{r})$ for all $b \in \mathbb{R}$ and $\mathbf{r} \in \mathbb{R}^3$.

Next, we use the direct method of calculus of variations (45) to establish existence of minimizers of $\tilde{F}[b]$. In view of Eq. 48, we have $\inf \tilde{F}[b] < +\infty$. The existence of minimizers then follows from coercivity and lower semicontinuity of $\tilde{F}[b]$ with respect to the weak convergence in $\mathring{W}^{1,2}(\mathbb{R}^3)$ and strong convergence in $L^1_{\mathrm{loc}}(\mathbb{R}^3)$ (45). Indeed, if $b_n \in \mathring{W}^{1,2}(\mathbb{R}^3)$ is a minimizing sequence, then for any $R > 0$, we have

$$
\begin{aligned}
+\infty > \tilde{F}[b_n] &= \int_{\mathbb{R}^3}\left[\frac{\lambda}{2}|\nabla b_n|^2 + \tilde{V}(b_n,\mathbf{r}) - V(b_{RBA}(\mathbf{r}),\mathbf{r})\right] d^3r\\
&\geq -\frac{4\pi}{3}CR^3 + \frac{\lambda}{2}\|\nabla b_n\|^2_{L^2(\mathbb{R}^3)}\\
&\quad + c\int_{B_R(0)}|b_n|\, d^3r
\end{aligned}
\tag{52}
$$

because by construction $\tilde{V}(b,\mathbf{r}) - V(b_{RBA},\mathbf{r}) \geq \max(0,\ c|b| - C)$ for some c, $C > 0$, and any $b \in \mathring{W}^{1,2}(\mathbb{R}^3)$. From Eq. 52, we obtain $\limsup_{n\to\infty}\|\nabla b_n\|^2_{L^2(\mathbb{R}^3)} < +\infty$, and after extraction of a subsequence, we have $\nabla b_n \rightharpoonup \nabla b$ in $L^2(\mathbb{R}^3;\ \mathbb{R}^3)$ and $b_n(\mathbf{r}) \to b(\mathbf{r})$ for almost every $\mathbf{r} \in \mathbb{R}^3$ for some $b \in \mathring{W}^{1,2}(\mathbb{R}^3)$. Then, by lower semicontinuity of the norm and Fatou's lemma applied to $V(b_n(\mathbf{r}),\ \mathbf{r})$, we get that $\liminf_{n\to\infty}\tilde{F}[b_n] \geq F[b]$, and so b is a minimizer of $\tilde{F}$. Furthermore, because $\tilde{F}$ is Fréchet differentiable with respect to compactly supported perturbations, we also have $D_\phi\tilde{F}[b] = 0$, i.e.,

$$\int_{\mathbb{R}^3}\left[\frac{\lambda}{2}\nabla b\ \cdot\nabla\phi+\tilde{V}'(b,\mathbf{r})\phi\right]d^3r=0,\ \forall\,\phi\in C_c^\infty\left(\mathbb{R}^3\right) \tag{53}$$

Having established existence of a minimizer of $\tilde{F}$, we now show that it satisfies Eq. 16 a posteriori. To show that $b\le b_+$, we define $\tilde{b}=\min(b_+,\max(b(\mathbf{r}),1-c_\infty/\nu))$; by Eq. 51, we have $\tilde{F}[\tilde{b}]\le\tilde{F}[b]$, and this inequality is strict unless $\tilde{b}=b$ almost everywhere in $\mathbb{R}^3$. Similarly, to establish $b\ge b_-$, we define $w=\min(0,b-b_-)\in\mathring{W}^{1,2}(\mathbb{R}^3)$ and note that $w=0$ in $B_{1/\nu}(0)$ or whenever $b\ge b_-$ in $B^{\,c}_{1/\nu}(0)$. Defining $\tilde{b}(\mathbf{r})=\max(b(\mathbf{r}),b_-(\mathbf{r}))$, we have

$$\tilde{F}[b]-\tilde{F}\left[\tilde{b}\right]=\int_{B^{\,c}_{1/\nu}(0)}\left[\frac{\lambda}{2}\nabla(b+b_-)\cdot\nabla w+V'(b_-(\mathbf{r}),\mathbf{r})\ w\right]d^3r \tag{54}$$

Using Eqs. 51 and 53 and the fact that $\nabla^2 b_-=0$ in $B^{\,c}_{1/\nu}(0)$ distributionally, integrating by parts we obtain

$$\tilde{F}[b]-\tilde{F}\left[\tilde{b}\right]=\frac{1}{2}\int_{B^{\,c}_{1/\nu}(0)}V'(b_-(\mathbf{r}),\ \mathbf{r})w\,d^3r\ge 0 \tag{55}$$

This inequality is strict unless $b=b_-$ almost everywhere in $\mathbb{R}^3$. Thus, the minimizer b satisfies Eq. 16 and hence is also a minimizer of $F[b]$ in $\mathring{W}^{1,2}(\mathbb{R}^3)$, subject to the constraint in Eq. 16.

We now establish uniqueness, regularity, and radial symmetry of the minimizer b. By Eq. 53, b satisfies Eq. 32 and is unique in this class because of the strict convexity of F ensured by Eq. 47. Namely, if b is a minimizer and $w\in\mathring{W}^{1,2}(\mathbb{R}^3)$ is such that $b+w$ still satisfies Eq. 16, with the help of Eqs. 53 and 45, we can write

$$F[b+w]-F[b]=\frac{1}{2}\int_{\mathbb{R}^3}\left[\lambda\left|\nabla w\right|^2+V''\left(\tilde{b}(\mathbf{r}),\ \mathbf{r}\right)w^2\right]d^3r \tag{56}$$

for some $\tilde{b}(\mathbf{r})$ between $b(\mathbf{r})$ and $b(\mathbf{r})+w(\mathbf{r})$. So, by Eqs. 56 and 47, we have $F[b+w]>F[b]$ for every $w(\mathbf{r})\neq 0$, and, therefore, $b(\mathbf{r})+w(\mathbf{r})$ is not a minimizer unless $w(\mathbf{r})=0$ almost everywhere in $\mathbb{R}^3$.

Then, by uniqueness of minimizer, we have $b(\mathbf{r})=b(|\mathbf{r}|)$ (with a slight abuse of notation), i.e., b is radially symmetric, as minimization may be carried out in the class of radial functions to obtain a radial solution of Eq. 32. Finally, elliptic regularity theory (44) yields that for any $1\le p<3$, we have $b\in W^{2,p}_{\mathrm{loc}}(\mathbb{R}^3)\cap C^\infty(\mathbb{R}^3/\{0\})$, and hence, by Sobolev embedding (40), we have $b\in C^{0,\alpha}(\mathbb{R}^3)$ for any $\alpha\in(0,1)$. In particular, $b(r)$ is continuous at $r=0$ and solves Eq. 18 for each $r>0$. Integrating this equation once near the origin yields

$$\frac{db}{dr}=\frac{C}{r^2}+\frac{b(0)}{2\lambda}+O(r^\alpha),\quad r\to 0 \tag{57}$$

for some $C\in\mathbb{R}$. In view of the square integrability of ∇b, we must have $C=0$, and so b is in fact Lipschitz continuous at the origin, which justifies Eq. 20. Lastly, boundedness of $F[b]$, Eq. 47, Lipschitz continuity of b, and decay of $b_{\mathrm{RBA}}-1$ at infinity yield $b(r)\to 1$ as $r\to\infty$.

AUTHOR CONTRIBUTIONS

V.M. conceived and designed the research project. V.M. and C.M. developed analytic methods. Y.C. and V.M. performed model analysis, numerical coding, numerical simulations, and simulation data analysis. All authors took part in the writing and review of the manuscript.

ACKNOWLEDGMENTS

The authors acknowledge valuable discussions with Vitaly Moroz.

This work was supported in part by National Science Foundation grant DMS-1517085 to V.M. and by National Science Foundation grant DMS-1908709 to C.M.

REFERENCES

1. Konieczny, V., M. V. Keebler, and C. W. Taylor. 2012. Spatial organization of intracellular Ca2+ signals. *Semin. Cell Dev. Biol.* 23:172–180.
2. Oheim, M., F. Kirchhoff, and W. Stühmer. 2006. Calcium microdomains in regulated exocytosis. *Cell Calcium.* 40:423–439.
3. Augustine, G. J., F. Santamaria, and K. Tanaka. 2003. Local calcium signaling in neurons. *Neuron.* 40:331–346.
4. Stanley, E. F. 2016. The nanophysiology of fast transmitter release. *Trends Neurosci.* 39:183–197.
5. Berridge, M. J., P. Lipp, and M. D. Bootman. 2000. The versatility and universality of calcium signalling. *Nat. Rev. Mol. Cell Biol.* 1:11–21.
6. Neher, E. 2000. Calcium buffers in flash-light. *Biophys. J.* 79:2783–2784.
7. Matthews, E. A., and D. Dietrich. 2015. Buffer mobility and the regulation of neuronal calcium domains. *Front. Cell. Neurosci.* 9:48.
8. Thurley, K., A. Skupin, …, M. Falcke. 2012. Fundamental properties of Ca2+ signals. *Biochim. Biophys. Acta.* 1820:1185–1194.
9. Dupont, G., M. Falcke, …, J. Sneyd. 2016. Models of Calcium Signalling.. Springer International Publishing, Cham, Switzerland.
10. Roberts, W. M. 1993. Spatial calcium buffering in saccular hair cells. *Nature.* 363:74–76.
11. Simon, S. M., and R. R. Llinás. 1985. Compartmentalization of the submembrane calcium activity during calcium influx and its significance in transmitter release. *Biophys. J.* 48:485–498.
12. Fogelson, A. L., and R. S. Zucker. 1985. Presynaptic calcium diffusion from various arrays of single channels. Implications for transmitter release and synaptic facilitation. *Biophys. J.* 48:1003–1017.
13. Chad, J. E., and R. Eckert. 1984. Calcium domains associated with individual channels can account for anomalous voltage relations of CA-dependent responses. *Biophys. J.* 45:993–999.
14. Neher, E. 1998. Usefulness and limitations of linear approximations to the understanding of Ca++ signals. *Cell Calcium.* 24:345–357.
15. Aharon, S., H. Parnas, and I. Parnas. 1994. The magnitude and significance of Ca2+ domains for release of neurotransmitter. *Bull. Math. Biol.* 56:1095–1119.
16. Bentele, K., and M. Falcke. 2007. Quasi-steady approximation for ion channel currents. *Biophys. J.* 93:2597–2608.
17. Rüdiger, S., J. W. Shuai, …, M. Falcke. 2007. Hybrid stochastic and deterministic simulations of calcium blips. *Biophys. J.* 93:1847–1857.
18. Smith, G. D. 1996. Analytical steady-state solution to the rapid buffering approximation near an open Ca2+ channel. *Biophys. J.* 71:3064–3072.
19. Smith, G. D., L. X. Dai, …, A. Sherman. 2001. Asymptotic analysis of buffered calcium diffusion near a point source. *SIAM J. Appl. Math.* 61:1816–1838.
20. Wagner, J., and J. Keizer. 1994. Effects of rapid buffers on Ca2+ diffusion and Ca2+ oscillations. *Biophys. J.* 67:447–456.
21. Bertram, R., G. D. Smith, and A. Sherman. 1999. Modeling study of the effects of overlapping Ca2+ microdomains on neurotransmitter release. *Biophys. J.* 76:735–750.

22. Bauer, P. J. 2001. The local Ca concentration profile in the vicinity of a Ca channel. *Cell Biochem. Biophys.* 35:49–61.

23. Naraghi, M. 1997. T-jump study of calcium binding kinetics of calcium chelators. *Cell Calcium.* 22:255–268.

24. Naraghi, M., and E. Neher. 1997. Linearized buffered Ca2+ diffusion in microdomains and its implications for calculation of [Ca2+] at the mouth of a calcium channel. *J. Neurosci.* 17:6961–6973.

25. Pape, P. C., D. S. Jong, and W. K. Chandler. 1995. Calcium release and its voltage dependence in frog cut muscle fibers equilibrated with 20 mM EGTA. *J. Gen. Physiol.* 106:259–336.

26. Stern, M. D. 1992. Buffering of calcium in the vicinity of a channel pore. *Cell Calcium.* 13:183–192.

27. Smith, G. D., J. Wagner, and J. Keizer. 1996. Validity of the rapid buffering approximation near a point source of calcium ions. *Biophys. J.* 70:2527–2539.

28. Neher, E. 1986. Concentration profiles of intracellular calcium in the presence of a diffusible chelator. Calcium Electrogenesis and Neuronal Functioning, Exp. Brain Res. 14. Springer-Verlag, pp. 80–96.

29. Coggins, M., and D. Zenisek. 2009. Evidence that exocytosis is driven by calcium entry through multiple calcium channels in goldfish retinal bipolar cells. *J. Neurophysiol.* 101:2601–2619.

30. Nguyen, V., R. Mathias, and G. D. Smith. 2005. A stochastic automata network descriptor for Markov chain models of instantaneously coupled intracellular Ca2+ channels. *Bull. Math. Biol.* 67:393–432.

31. Montefusco, F., and M. G. Pedersen. 2018. Explicit theoretical analysis of how the rate of exocytosis depends on local control by Ca^{2+} channels. *Comput. Math. Methods Med.* 2018:572109712.

32. Trommershäuser, J., R. Schneggenburger, …, E. Neher. 2003. Heterogeneous presynaptic release probabilities: functional relevance for short-term plasticity. *Biophys. J.* 84:1563–1579.

33. Matveev, V. 2018. Extension of rapid buffering approximation to Ca^{2+} buffers with two binding sites. *Biophys. J.* 114:1204–1215.

34. Matveev, V. 2016. Padé approximation of a stationary single-channel Ca^{2+} nanodomain. *Biophys. J.* 111:2062–2074.

35. Falcke, M. 2003. On the role of stochastic channel behavior in intracellular Ca2+ dynamics. *Biophys. J.* 84:42–56.

36. Falcke, M. 2003. Buffers and oscillations in intracellular Ca2+ dynamics. *Biophys. J.* 84:28–41.

37. Muatjetjeja, B., and C. M. Khalique. 2011. Exact solutions of the generalized Lane–Emden equations of the first and second kind. *Pramana J. Phys.* 77:545–554.

38. Ablowitz, M. J., and A. S. Fokas. 2003. Complex Variables. Cambridge University Press, Cambridge, UK.

39. Gillespie, D. 2020. Simulating diffusion from a cluster of point sources using propagation integrals. *Eur. Biophys. J.* 49:385–393.

40. Evans, L. C. 1998. Partial Differential Equations: Graduate Studies in MathematicsVolume 19. American Mathematical Society, Providence, RI.

41. Faas, G. C., B. Schwaller, …, I. Mody. 2007. Resolving the fast kinetics of cooperative binding: Ca2+ buffering by calretinin. *PLoS Biol.* 5:e311.

42. Chin, D., and A. R. Means. 2000. Calmodulin: a prototypical calcium sensor. *Trends Cell Biol.* 10:322–328.

43. Schwaller, B. 2014. Calretinin: from a "simple" Ca(2+) buffer to a multifunctional protein implicated in many biological processes. *Front. Neuroanat.* 8:3.

44. Gilbarg, D., and N. S. Trudinger. 1983. Elliptic Partial Differential Equations of Second Order. Springer-Verlag, Berlin.

45. Struwe, M. 2000. Variational Methods: Applications to Nonlinear Partial Differential Equations and Hamiltonian Systems. Springer, Berlin.